Flight Test Results of an Active Flutter Suppression System

John W. Edwards*
NASA Langley Research Center, Hampton, Virginia

Flight flutter test results of the first aeroelastic research wing of NASA's Drones for Aerodynamic and Structural Testing (DAST) Program are presented. The implementation of the flutter suppression system and the flight test operation are described. The conduct of the flutter testing and the near-real-time damping estimation algorithm are also described in detail. Flight data were obtained at Mach numbers up to 0.91 and were of high quality. Response to fast frequency sweep excitation provided reliable damping estimates and the open-loop flutter boundary was well defined. Evidence of angle-of-attack effects upon damping at high transonic Mach numbers is also presented. While the flutter suppression system provided augmented damping at speeds below the flutter boundary, an error in the implementation of the system gain caused the system to be less stable than predicted and the vehicle encountered system-on flutter on the third flight.

Nomenclature

a_z	= normal acceleration, g
f	= frequency, Hz
F	= Fourier transform
G_c	= common filter transfer function
G_s, G_a	= symmetric and antisymmetric filter transfer functions, respectively
H	= altitude, m (ft)
K	= FSS gain
M	= Mach number
M_f	= flutter Mach number
S_{xy}	= cross spectrum between x and y
$s=\sigma+i\omega$	= Laplace transform variable, rad/s
t, T	= time, s
u	= intermediate FSS variable
α	= angle of attack, deg
δ	= aileron position, deg
ζ	= damping ratio
$\phi_{c.g.}$	= center of gravity roll acceleration, rad/s^2
$d\phi/d\omega$	= rate of change of phase, deg/deg s^{-1}

Subscripts

c	= command variable
c.g.	= center of gravity
l, r	= left, right
s, a	= symmetric, antisymmetric
tm	= tip mass

Introduction

CORRELATION of theoretical predictions and experimental flight test results of aeroelastic effects in the transonic speed range are of great interest since transonic effects frequently are critical in aircraft design. The objective of NASA's Drones for Aerodynamic and Structural Testing (DAST) Program[1] is to pursue investigations of this area using a series of aeroelastic research wings (ARW) which will be flight tested on a modified Firebee II target drone vehicle fuselage utilizing the remotely piloted research vehicle (RPRV) technique.[2] DAST is a joint program between NASA's Langley and Dryden Flight Research centers. The flight tests described in this paper were supported under contract by the Boeing Military Aircraft Company, Wichita division. The first wing to be tested in the DAST program, denoted the ARW-1, is a swept-back transport-type wing with a supercritical airfoil shape whose design point is $M=0.98$ at 13.72 km (45,000 ft). The primary research objective of the ARW-1 is to investigate systems synthesis and analysis techniques for the active control of flutter utilizing an onboard flutter suppression system (FSS). A secondary objective is to validate analysis techniques for aerodynamic loads predictions. The use of the RPRV technique poses special concerns in the conduct of the flight testing since testing time per flight is quite limited and a much higher probability of vehicle loss is an accepted risk as opposed to piloted flight testing. In this light, the flight testing of the ARW-1 had the additional objective of developing flutter test techniques for use under these constraints. This paper presents details of the flutter test technique development and of the implementation of the FSS on the vehicle. Frequency and damping estimates obtained from flight tests using this near-real-time estimation technique are compared with predictions from Ref. 3. Newsom and Pototsky[3] present details of the mathematical modeling and FSS design, while Bennett and Abel[4] present more detailed frequency and damping estimates obtained using a postflight parameter estimation technique. Three flight operations of the ARW-1 have been conducted. Owing to an error in the implementation of the gain of the FSS the vehicle experienced flutter on the third flight resulting in the separation of the right wing and ground impact.

DAST System Description

The first wing to be tested in the DAST program is a 6.8 aspect ratio, swept-back, transport-type wing with a supercritical airfoil shape. Design of this wing and the active flutter suppression system was performed under contract and is described in Refs. 1 and 5. While the supercritical wing design point was at $M=0.98$ and $H=13.72$ km (45,000 ft), the achievement of the active flutter suppression experiment goal of a 20% increase in the unaugmented flutter speed was to be accomplished at the much lower altitudes of 3.05-4.57 km (10,000-15,000 ft). The basic Firebee drone has no wing control surfaces and is controlled by collective and differential horizontal stabilizer and rudder deflections. The DAST ARW-1 retained this method of flight control, thus leaving the wing ailerons free to perform the flutter suppression function. Figure 1 shows the overall planform of the vehicle. The wing was constructed with front and rear steel spars with torsional stiffness provided by fiberglass skins. The wing leading and trailing edges are constructed of fiberglass and the wing span is 4.30 m (14 ft). To produce wing flutter

Presented as Paper 81-0655 at the AIAA Dynamics Specialists Conference, Atlanta, Ga., April 9-10, 1981; submitted April 27, 1981; revision received May 27, 1982. This paper is declared a work of the U.S. Government and therefore is in the public domain.

*Head, Unsteady Aerodynamics Branch. Member AIAA.

within the operational envelope of the vehicle, torsional stiffness was intentionally reduced by orienting the fiberglass filaments at 0 and 90 deg to the front spar and by the addition of wing-tip ballast weights of 0.91 kg (2 lb).

Tip Mass Release System

Automatic or manual jettison of the tip masses was viewed as a desirable feature in order to aid recovery from inadvertent large amplitude wing oscillations and this was accomplished by sensing wing-tip accelerations and firing a pyrotechnic device to allow the lead shot ballast to be thrown out of its container. The automatic firing sequence was initiated when the rms wing-tip acceleration exceeded a 10.6g threshold, with the actual firing occurring after a delay determined by the rms acceleration level in excess of the threshold. The threshold g level was selected based on the acceleration causing saturation of the FSS compensator. It was predicted that structural failure of the wing would not occur until wing-tip accelerations reached 64g and that compressive stress of the wing skin along the 25% chord line was the critical stress. In addition to this automatic mode, a backup manual tip mass release capability was provided to the flutter test engineers.

Mathematical Model

A NASTRAN finite-element model of the ARW-1 and Firebee fuselage-empennage was constructed and ground vibration tests (GVT) were performed on the vehicle. Table 1 presents comparisons of the frequencies obtained indicating fair to good agreement. The differences in first wing-bending mode frequencies (0.5 Hz for symmetric and 1.2 Hz for antisymmetric) are larger than is desirable. However, attempts to refine the NASTRAN model have not produced significant improvement in the agreement with the GVT results.

Aeroelastic analysis, utilizing a doublet-lattice computer program predicted classical wing-bending-torsion flutter in both symmetrical and antisymmetrical modes at nearly identical altitude/Mach number conditions. In both cases, the lower-frequency first wing-bending modes near 10 Hz combined with the bending-torsion modes near 30 Hz to produce flutter modes in the range of 15-20 Hz, with the lower-frequency bending modes becoming the unstable flutter modes.

Instrumentation

Response measurements were telemetered to the ground via a pulse code modulation (PCM) telemetry system. The PCM system consisted of a 19 word mainframe with each 10-bit word sampled 500 times per second. Ten of the mainframe words transmitted flutter critical sensor signals at the maximum rate of 500 samples per second, while the remaining mainframe words were subcommutated in order to transmit the remaining signals. The ten flutter parameters were six wing-tip accelerations, both aileron positions, differential hydraulic pressure, and flutter test excitation signal. All of these signals were analog prefiltered to prevent aliasing, with most channels incorporating 70-Hz sixth-order filters.

Table 1 Normal mode frequencies predicted by NASTRAN analysis and measured during ground vibration test

Mode	NASTRAN f, Hz	GVT f, Hz
Symmetric		
First wing bending	9.1	9.6
First fuselage bending	16.5	16.2
Wing bending torsion	29.6	29.1
	34.0	31.2
	39.8	40.6
	48.6	48.5
Antisymmetric		
First wing bending	12.3	13.5
First fuselage yaw	21.7	19.3
Wing bending torsion	30.0	27.0
	34.2	31.0
	36.0	...
	48.3	48.4

Flutter Suppression System

The flutter suppression system (FSS) was designed and fabricated under contract[5] and is implemented as an onboard analog system as shown in Fig. 1. No redundancy was provided for any of the system's sensors, electronics, or actuators. The 23% chord ailerons have a 0.254-m (10-in.) span and are located just inboard of the wing closure rib. During the FSS design study combinations of two accelerometers on each wing tip were considered for sensing wing motion, but a single accelerometer mounted on the rear spar at the outboard aileron edge was chosen.

Miniaturized rotary vane hydraulic actuators[6] were used to control the aileron motion. Figure 1 shows the location of the hydraulic pump and accumulator and the electrohydraulic servovalves which are separated from the actuators by 2.14 m (7 ft) of hydraulic tubing. The control surfaces were stabilized with position and differential pressure feedback. The bandwidth of these control surfaces proved to be a critical variable in the FSS design. Preliminary design of the FSS was accomplished assuming a mathematical model of the controls with a bandwidth of 100 Hz. When the controls were fabricated and bench tested, a 70-Hz bandwidth was achieved and, when the control surfaces were installed in the wing, the final bandwidth was 50 Hz. The resulting phase lag ($\sim$30 deg at 20 Hz) severely compromised the original FSS compensator design.

Since suppression of both symmetrical and antisymmetrical flutter modes was required, the FSS compensator was implemented via the summing and differencing networks shown schematically in Fig. 2. The left and right wing-tip accelerations, a_{zl} and a_{zr}, were passed through common filters, G_c, and then summed to yield the symmetric intermediate signal, u_s, and differenced to yield the antisymmetric in-

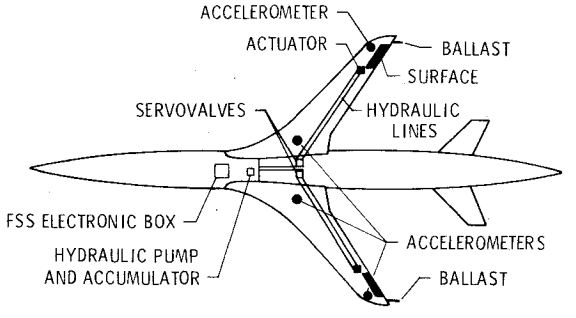

Fig. 1 Planform of the DAST ARW-1 showing the flutter suppression system installation.

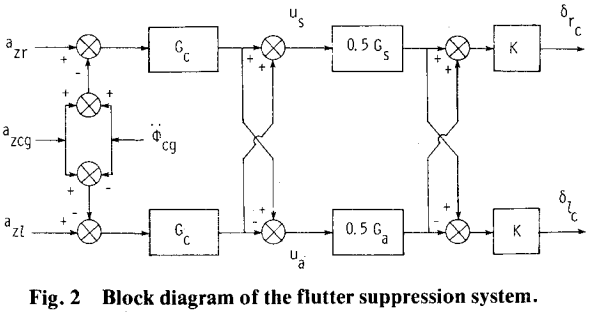

Fig. 2 Block diagram of the flutter suppression system.

termediate signal, u_a. In order to isolate the FSS dynamics from the lower-frequency rigid body dynamics, the center of gravity acceleration, $a_{zc.g.}$, was subtracted from each signal and the fuselage roll acceleration, $\ddot{\phi}_{c.g.}$, was added to a_{zl} and subtracted from a_{zr}. The intermediate signals, u_s and u_a, were filtered by G_s and G_a, and the resulting signals summed, differenced, and multiplied by the gain, K, to yield the left and right aileron servo commands δ_{l_c} and δ_{r_c}. The mathematical model considered only a half-airplane with boundary conditions along the fuselage centerline accounting for the full airplane. Consequently, the resulting compensator gain is specified for a single a accelerometer feedback and the factor of 0.5 is required to account for the two accelerometers, one on each wing tip. The original FSS compensator implementation included the factor of 0.5 multiplying G_s and G_a to properly implement the compensator analyzed with the mathematical model. In addition, K was set equal to unity. Although predictions indicated that the reduced control surface bandwidth mentioned above would not allow achievement of a 20% increase in flutter speed, it was adequate for flutter suppression at speeds moderately above the flutter boundary and it was retained for the first two flight operations. During this time period, a redesign of the FSS was performed incorporating the reduced bandwidth characteristics of the servoactuator system. The analyst, not realizing that the 0.5 correction was already incorporated in the G_s and G_a filters, provided the new compensator filters G_c, $0.5G_s$, $0.5G_a$, and, in addition, specified $K=0.5$. These filters, implemented for the third ARW-1 flight, are

$$G_c = \frac{2.25\times 10^6 s(s^2+76s+295^2)(s^2+120s+306^2)}{(s+2)(s+295)^2(s^2+240s+342^2)(s+1500)^2}$$

$$\times \frac{(s^2+60+1037^2)(s^2+76s+1269^2)}{(s^2+300s+1037^2)(s^2+500s+1269^2)}$$

$$G_s = \frac{-1.6(s^2+100s+71^2)(s^2+100s+168^2)}{(s^2+100s+58^2)(s^2+100s+112^2)}$$

$$G_a = \frac{-2.528(s^2+100s+158^2)}{(s^2+80s+D)}$$

The antisymmetric FSS contained the parameter D, in G_a, which was scheduled on dynamic pressure and resulted in a 70% increase in gain for the antisymmetrical compensator in going from a dynamic pressure of 31,122-43,523 N/m^2 (650-909 psf).

Figure 3 indicates the predicted performance of the new symmetrical FSS, showing the loci of the open-loop bending and bending-torsion modes vs Mach number. The bending mode goes unstable (flutters) at $M\sim 0.83$ at a frequency of 100 rad/s (16 Hz), while the torsion mode becomes heavily damped as Mach number increases. Also shown, near $\omega=100$ rad/s is the locus of the first fuselage bending mode, which indicates considerable coupling with the bending mode near M_f. At $M=0.75$, 0.85, and 0.90 the effect of increasing the gain, K, from 0.0 to 1.0 is shown. Acceptable damping is achieved at all Mach numbers for nominal gain ($K=1.0$), but the bending mode is predicted to be unstable above $M=0.85$ at one-half nominal gain. The torsion mode is heavily damped by the FSS at all Mach numbers.

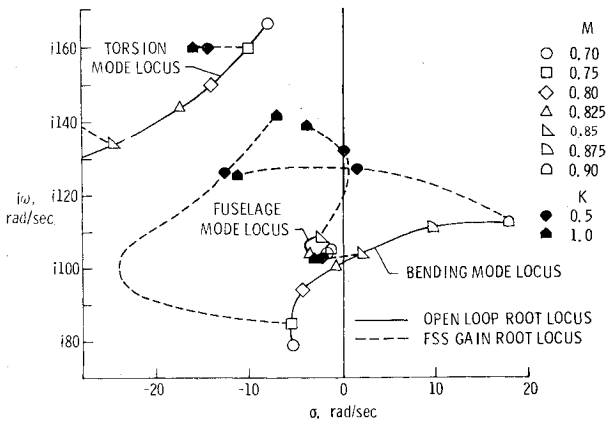

Fig. 3 Predicted open-loop flutter mode root locus and flutter suppression system gain root locus at $H=4.75$ km (15,000 ft).

Flutter Test Technique

The flight test operations utilized the RPRV technique.[2] Flight test time for each flight varied between 15 and 30 min, depending on the flight conditions chosen. The vehicle was operated with feedback augmentation in all axes and the pilot was able to maintain the vehicle to within ± 0.01 Mach number and ± 76.2 m (± 250 ft) altitude of desired test conditions. Two additional ground-based facilities for monitoring and controlling the progress of the flight test are the Control Room and the Structural Analysis Facility. The Control Room contains strip charts for monitoring the vehicle rigid body stability and control functions and operational functions, radar plot boards for monitoring vehicle flight path, and communication equipment required to coordinate the aircraft involved in the test. The flutter test monitoring was performed in a separate location, the Structural Analysis Facility (SAF).

Structural Analysis Facility

The SAF is a dedicated facility configured to perform structural dynamic and flutter testing. Six flutter test engineers in the SAF participated in the flight testing. One engineer served as flutter test director, overseeing the monitoring of the test and communicating directly with the test pilot. The command capabilities of the control panel are 1) FSS-on or -off, 2) auxiliary filter in or out, 3) tip mass jettison, 4) frequency sweep or pulse excitation, 5) symmetric or antisymmetric excitation, and 6) low or high amplitude excitation. In addition, a remote tip mass jettison "pickle switch" was provided to the test engineer observing the critical flutter strip chart.

The spectrascope was utilized as a "quick-look" instrument, providing spectral estimates of selected signals over a broad frequency bandwidth. It thus supplemented the Fourier analyzer, which was dedicated to the estimation of frequencies and dampings near the anticipated flutter frequency of 20 Hz. Six channels were input to the Fourier analyzer at 500 samples per second (three wing-tip accelerations, two aileron positions, and the FSS excitation signal) using a multiplexor preprocessor. The analyzer computed estimates of dominant mode frequency and damping and displayed results on a cathode ray tube display unit.

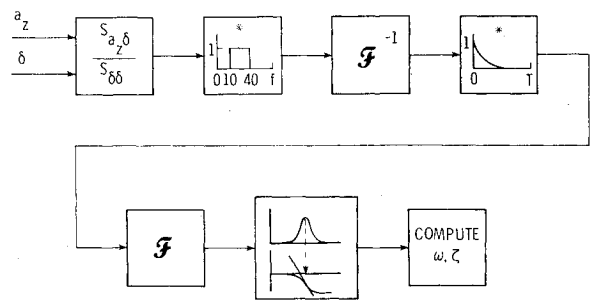

Fig. 4 Functional diagram of the near-real-time transfer function and damping ratio estimation algorithm.

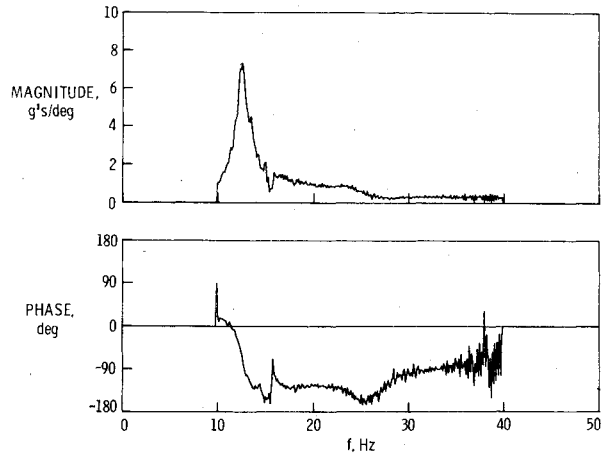

Fig. 5 Raw transfer function estimate of a_{zl} due to δ_l symmetrical frequency sweep at $M=0.74$ and $H=4.57$ km (15,000 ft).

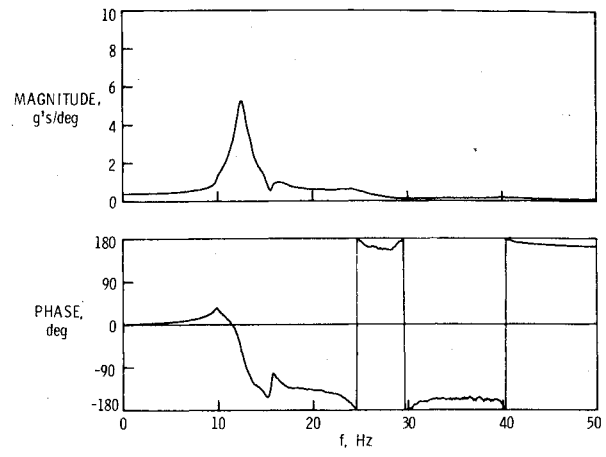

Fig. 6 Smoothed transfer function estimate of a_{zl} due to δ_l for symmetrical frequency sweep at $M=0.74$ and $H=4.57$ km (15,000 ft).

FSS Excitation and Damping Estimation Technique

Flight flutter test techniques[7,8] have traditionally relied heavily upon long duration testing to obtain random turbulence excited response or upon slow frequency sweeps to obtain quasi-steady-state forced response. The goal in any case is to obtain reliable estimates of critical mode damping to allow flight testing to proceed. The introduction of minicomputer based Fourier analyzers utilizing fast Fourier transform techniques, coupled with the measurement of both the input forcing function (control surface displacement) and the response (wing acceleration) allows the use of transfer function analysis and greatly reduces test time. Quasi-steady-state test methods are no longer necessary, and fast frequency sweeps were chosen as the preferred method of excitation. The excitation was summed with the FSS feedback signals allowing the ailerons to be used both to excite the wing and to control the flutter mode. A logarithmic frequency sweep function was implemented as

$$\delta_c = A\sin[a\omega_0 \ell n(a-t)]$$

where $a=\omega_l T/(\omega_l-\omega_0)$, with ω_0 and ω_l the starting and stopping frequencies and T the sweep duration. Sweep amplitudes, A, of 1 and 2 deg were available. Since the predicted flutter frequency was near 20 Hz, the starting and stopping frequencies were chosen to be 10 and 40 Hz. A sweep duration of 7 s was chosen based upon an 8-s period required for the Fourier analyzer to take 4096 data points at the maximum rate of 500 samples per second. This allowed 0.5-s settling time at the start and end of the sweeps for transients to die out. In addition, the sweep command amplitude was tapered at the beginning and end to eliminate transients.[9] In addition to the sweeps, a capability to pulse the ailerons was included so that the test engineers could monitor transient responses. The pulse consisted of a single cycle of a 20-Hz sine wave with an amplitude of either 1.7 or 3.4 deg.

Owing to the limited flight time available, the DAST flight flutter testing required a fast method of obtaining a single mode damping estimate with a minimum of operator interaction. The near-real-time damping estimation technique used is illustrated in Fig. 4. The raw transfer function estimate of acceleration response due to aileron motion was obtained as the cross spectrum, $S_{a_z\delta}$, divided by the input autospectrum, $S_{\delta\delta}$. Since there was little input power outside the range of the frequency sweep, the function was set to zero below 10 Hz and above 40 Hz.

A single raw transfer function estimate is frequently not very useful owing to noise, truncation, and the effects of unknown forcing functions. When test time is available, repeated tests and averaging are used to provide reliable estimates. When averaging is not feasible, as in the DAST program, ad hoc techniques of smoothing the raw transfer function estimates are sometimes used. The technique used to smooth the DAST data was the exponential window.[10] Inverse Fourier transformation of the transfer function, F^{-1}, gives an estimate of the impulse response function. Multiplication of this estimate by $\exp(-at)$ forces the function to zero and minimizes extraneous effects at large values of t. Fourier transformation, F, of the windowed impulse response function then yields the smoothed transfer function from which frequency and damping may be estimated. The effect of the exponential window on the estimated damping may be calculated, a point in favor of this approach. Figures 5 and 6 indicate the effect of the exponential window on a transfer function estimate of a_{zl}/δ_l from a symmetrical open-loop sweep at $M=0.74$ and an altitude of 4.57 km (15,000 ft). The magnitude and phase of the raw transfer function are shown in Fig. 5 and the smoothed function is shown in Fig. 6. An exponential window of $\exp(-t)$ was used. The very lightly damped bending mode is seen at $f=13.3$ Hz. The smaller mode near 16 Hz is the first fuselage bending mode.

The smoothed transfer function may now be used to estimate the damping of the dominant resonant peak. Various techniques are available for estimating damping but a technique that could be automated was desired. The technique chosen was to search for the peak magnitude of the transfer function and at the frequency of the peak magnitude determine the damping from the estimated slope of the phase curve. The damping of the single-degree-of-freedom transfer function

$$H(s)=\frac{\omega_0^2}{s^2+2\zeta\omega_0 s+\omega_0^2}$$

is given by

$$\zeta=-\left(\omega_0\frac{d\phi}{d\omega}\bigg|_{\omega=\omega_0}\right)^{-1}$$

where

$$\frac{d\phi}{d\omega}\bigg|_{\omega=\omega_0}$$

is the slope of the phase curve at resonance. The frequency of the peak resonance was determined via a least-squares curve fit of a quadratic function to the five points adjacent to the peak magnitude and the slope of the phase curve was determined similarly using a five-point least-squares curve fit of a cubic function to phase data points. This near-real-time damping estimation technique was implemented in the Fourier analyzer in a fully automatic mode.

The first two flights utilized the program with the maximum data block size available in order to obtain the best

resolution possible (block size of 4096, 500 samples per second). This block size required 15 s to process each transfer function estimate and obtain frequency and damping estimates. Postflight data processing indicated equivalent results could be obtained with a block size of 1024 and a sample rate of 100 samples per second. This technique was used on the third flight and reduced the processing time to 5 s.

Flight testing was accomplished at constant altitude using preplanned Mach number increments of 0.05 and 0.025. The test procedure at each flight condition depended upon whether the flight condition was above or below the open-loop flutter Mach number. At conditions below the flutter boundary, a sequence of four sweeps was used: 1) symmetric, FSS-off, 2) antisymmetric, FSS-off, 3) antisymmetric, FSS-on, and 4) symmetric, FSS-on. Beyond the open-loop flutter boundary, the FSS could obviously not be turned off and only the two FSS-on sweeps were to be obtained.

The left and right wing aileron positions and accelerations were summed and differenced to provide signals for symmetric and antisymmetric processing. For FSS-off tests, transfer functions of acceleration due to aileron motion provided open-loop damping estimates while transfer functions of acceleration due to the excitation signal provided closed-loop damping estimates for the FSS-on tests. For the FSS-on sweeps, transfer function estimates were also obtained for wing acceleration due to aileron motion in an attempt to determine the open-loop damping from closed-loop data. This technique requires that the data be relatively noise-free and be free from extraneous input such as atmospheric turbulence.

Flight Test Results

It was anticipated that the objectives of the flutter suppression tests could be accomplished in six flights.[1] Testing was planned at low, medium, and high altitudes with the FSS design point to be reached on the fourth flight at 3.05 km (10,000 ft). The first flight was to be devoted to subcritical testing, exercising the FSS at Mach numbers no closer than 0.1 M to the predicted flutter boundary. The second flight was to test 0.05 M past M_f with the FSS engaged. Figure 7 shows the test points which were achieved on the three flights of the ARW-1 and gives the predicted flutter boundaries which were used to plan the third flight. Boundaries are shown for FSS-off and -on and for the tip masses on and off. The open symbols in Fig. 7 denote test points at which only FSS-off testing was accomplished while the half-open symbols indicate test points for both FSS-off and FSS-on testing. Solid symbols indicate those points which were predicted to be at or above the flutter Mach number and thus only FSS-on testing was done.

The first flight encountered several difficulties, including failure of the FSS hydraulic pump and intermittent loss of the telemetry uplink command signal. Figure 7 indicates the highest Mach number achieved was $M=0.75$ at 4.88 km (16,000 ft) and, while little test data was gathered, very light damping of the antisymmetric bending mode was observed.

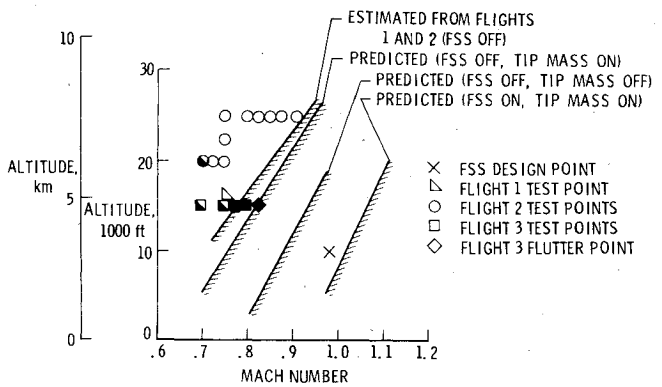

Fig. 7 Flight envelope of the ARW-1 showing predicted flutter boundaries and flight-test points.

In the second flight, data were obtained at ten test points at 6.10 (20,000) and 7.62 km (25,000 ft) and at Mach numbers from 0.7 to 0.91. At the first test point on flight 2 [$M=0.7$ and 6.10 km (20,000 ft)] a 200-Hz limited amplitude instability was observed when the FSS was engaged. Similar instabilities had been encountered during ground testing and were caused by the interaction of the high bandwidth aileron control systems with the structure. These hydraulic resonances observed during ground testing were controlled with notch filters and when they were observed in flight it was decided to terminate FSS-on testing for the remainder of the flight even though the FSS was providing excellent control of the bending modes at the first test point. The duration of the flight was 25 min and test data were obtained from 14 frequency sweeps and 177 pulses. The flight resulted in a very good definition of the flutter boundary at $M\sim 0.92$ and 7.62 km (25,000 ft), whereas analysis had predicted $M_f=0.95$ at this altitude. This led to the incorporation of a correction factor[3] to the unsteady airloads which was based on the ratio of the static rigid body lift curve slope measured during a wind tunnel test to its predicted value. This correction factor was included in the predictions used in the planning of flight 3.

The objective of flight 3 was to test 0.05 M past the flutter boundary at 4.57 (15,000) and 6.10 km (20,000 ft). Flight planning was based upon the more conservative flutter boundary estimated from flights 1 and 2 (Fig. 7) rather than the predicted flutter boundary and $M=0.825$ km was the highest Mach number to be tested at 4.57 km (15,000 ft). The duration of flight 3 prior to the flutter incident was 10 min during which four test points were achieved and data were obtained from 12 frequency sweeps and 75 pulses.

Frequency Sweep Data

The quality of the flight test data obtained from the ARW-1 was extremely good. The average rms background acceleration level was approximately 0.25g, while responses due to FSS excitation signals ranged up to 10g. Consequently, the signal-to-noise ratio was very high. Figure 8 shows time histories of aileron position and wing-tip acceleration during FSS-off and -on, symmetric, low amplitude frequency sweeps for flight 3 at $M=0.74$ and 4.57 km (15,000 ft). The resonance of the bending mode is clearly seen in the FSS-off sweep of Fig. 8a, whereas this mode is heavily damped in the FSS-on sweep of Fig. 8b. Figure 9 gives the frequencies and dampings obtained during flight 2 at 7.62 km (25,000 ft) by the near-real-time damping estimation technique. The frequencies near 25 Hz are from the more highly damped torsion modes and were determined following the flight. The faired curve through the data points gives a very good definition of the FSS-off flutter boundaries between $M=0.91$ and 0.92 for both symmetric and antisymmetric modes. A point of interest is that the static pressure data from this altitude indicates that the wing tips were downloaded above $M=0.85$. Thus, at these off-design conditions for this supercritical airfoil, the effective angle of attack at the tips was negative.

The elimination of FSS-on testing due to the 200 Hz instability during flight 2 left ample flight time for repeat testing at $M=0.85$, 0.875, and 0.9 and Fig. 9 indicates very good repeatability of the damping estimates at these Mach numbers. Also, at $M=0.85$, data were obtained from high amplitude (± 2 deg) frequency sweeps and the resulting damping estimates shown in Fig. 10 indicate no appreciable amplitude effect at this Mach number.

Between flights 2 and 3 the modified FSS compensator was implemented, including the one-half gain error described earlier. Figure 7 indicates test points at 4.57 km (15,000 ft) and $M=0.7$, 0.75, 0.775, and 0.8 which were achieved prior to the flutter incident at $M=0.825$. No instability was an-

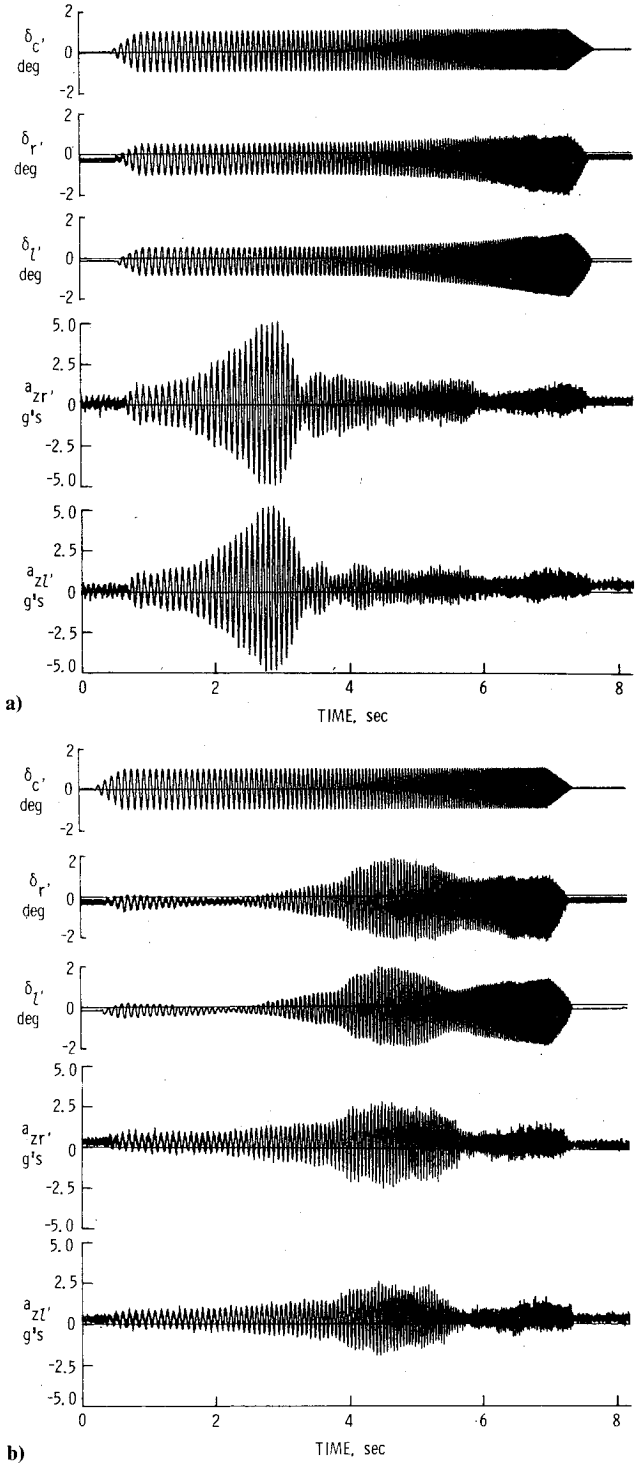

Fig. 8 Response to symmetrical frequency sweep excitation at $H = 4.56$ km (15,000 ft) and $M = 0.74$ (flight 3). a) FSS-off. b) FSS-on.

ticipated on this flight (nominal gain $M_f = 1.06$ at this altitude, Fig. 7) and the flight-path acceleration used to proceed between test points resulted in times of 12-15 s to achieve Mach number increments of 0.025.

The results of the near-real-time damping estimates obtained from sweeps on flight 3 are presented in Figs. 10 and 11. Comparisons between predictions and flight test results are shown as s-plane root loci to better explain the effects of FSS-off and -on and one-half nominal gain. Figure 10 presents the antisymmetric results. The predicted FSS-off root loci of the bending and torsion modes are shown for $0.7 < M < 0.90$. Also shown are the predictions of the FSS-on dominant mode root loci for nominal and one-half gain. The

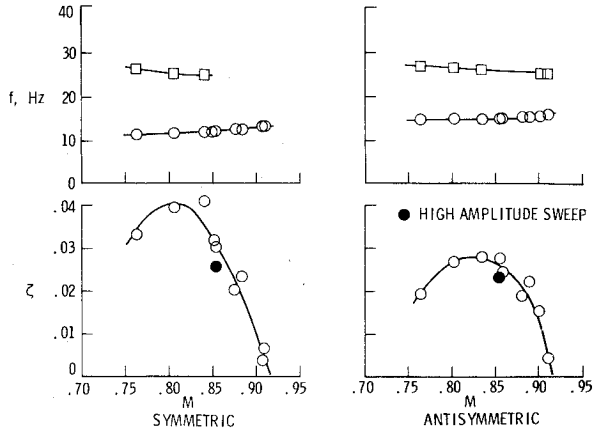

Fig. 9 Bending mode frequency and damping at $H = 7.62$ km (25,000 ft).

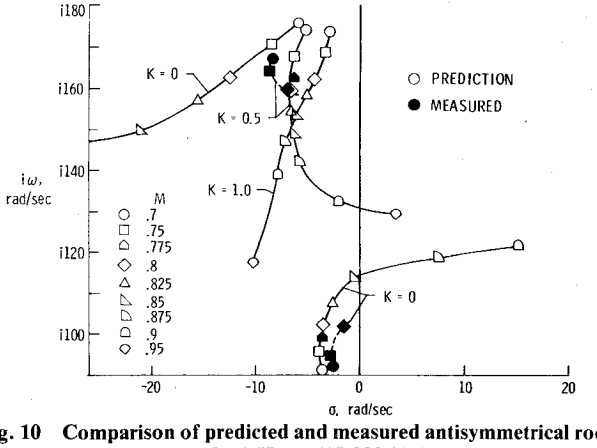

Fig. 10 Comparison of predicted and measured antisymmetrical root loci vs Mach number at $H = 4.57$ km (15,000 ft) (open symbols denote predictions, closed symbols denote flight test results).

effect of the FSS upon the bending mode is to heavily dampen the mode and lower its frequency for Mach numbers less than M_f while the torsion mode is slightly destabilized. Figure 10 indicates that the antisymmetric mode is predicted to be stable even at one-half gain for Mach numbers up to 0.9. The flight-test frequency and damping estimates are given by solid symbols and indicate good agreement with these predictions. The flight-test open-loop bending mode frequencies shown near 100 rad/s agree well with predictions although the damping is overpredicted. The flight test results appear to project to an open-loop flutter boundary at a lower Mach number and frequency than predicted. The results from the third test point at $M = 0.775$ are believed to be less reliable than the others since extraneous wing responses, possibly due to atmospheric turbulence, were observed at this test point. Also, the FSS-off results for the $M = 0.775$ and 0.8 cases are from FSS-on sweep data.

The FSS-on antisymmetric response of the wing correlates well with predictions, as shown by the closed symbols near 160 rad/s in Fig. 10. Again the $M = 0.775$ result appears to be erratic, while the other three estimates are close to their predicted values, especially at $M = 0.8$. Reference 4 presents frequency and damping estimates of both the bending and torsion modes obtained from a postflight analysis, while Ref. 3 gives more details of the predicted response.

Similar information for the symmetric case is presented in Fig. 11. The estimated FSS-off frequencies and dampings near 80 rad/s are lower than predicted and project to an open-loop flutter Mach number lower than predicted, but the trend toward instability is in reasonable agreement. As with the antisymmetric case, the results from $M = 0.775$ appear erratic.

The effect of the one-half gain error is much more severe in this case, with instability predicted above $M=0.85$ with FSS-on. Also, the rate of change of damping of the one-half gain locus indicates a very violent flutter onset between $M=0.825$ and 0.85, whereas the nominal gain locus, which was anticipated during the flight, indicates increased damping above $M=0.825$.

The near-real-time FSS-on damping estimates for $M=0.7$ and 0.75 were off-scale and are not shown. The more accurate postflight damping estimates of Ref. 4 for these Mach numbers give values of $\zeta \sim 0.13$ and $\omega \sim 125$ rad/s corresponding to a root location at $s \sim -16 \pm i125$ rad/s, close to the predicted location. Thus the near-real-time damping estimation appears to be unreliable for damping ratios greater than 0.10. The frequency and damping estimate obtained from the sweep data at $M=0.8$ and the frequency of the flutter mode at $M=0.825$ correlate very well with the trend of the predicted one-half gain locus. Particularly interesting is the fact that the doublet-lattice aerodynamic theory predicted the control surface effectiveness very well. The math model predicted an increase of bending mode frequency from $\omega=95$ to 131 rad/s for the one-half gain FSS at $M=0.8$ whereas the flight data show an increase from 87 to 125 rad/s.

Pulse Data

The large number of pulse responses obtained were analyzed following the flights to determine their usefulness in providing damping estimates. The pulses were also of interest in studying the effect of angle of attack upon damping at transonic speeds since such effects have been noted in other studies, especially for supercritical airfoils. A typical pulse response is shown in Fig. 12 and the damping estimates for the FSS-off, antisymmetric pulse data taken at 7.62 km (25,000 ft) are plotted vs Mach number in Fig. 13. There is a good deal of scatter in the estimates at a given Mach number and comparison with the frequency sweep results in Fig. 10 shows that the damping estimates obtained from the pulse data do not indicate the approach to the flutter boundary at $M=0.92$ when plotted vs Mach number. Similar results were obtained from the symmetric, FSS-off pulses.

To investigate possible effects of angle of attack upon damping, the pulse damping ratios obtained from narrow Mach number ranges were crossplotted against angle of attack. Figure 14 presents symmetric and antisymmetric results for two Mach number ranges for FSS-off pulse data taken at 7.62 km (25,000 ft). The flagged symbols indicate high amplitude pulses and, as with the sweep data, no significant amplitude effects are apparent. The damping estimates obtained from the frequency sweeps at $M=0.875$ and 0.9 are also plotted vs the angle of attack observed as the sweep passed through the resonant frequency. The most interesting trend is seen in the antisymmetric case for $0.893<M<0.911$ where an apparent correlation is seen between damping and angle of attack. The damping ratio decreases from $\zeta=0.03$ to 0.01 as the angle of attack decreases 0.3 deg and the same trend is seen in the sweep results. The symmetric pulse damping results for the same Mach number range do not present as clear a trend, owing to the wide range in damping at 1.9-deg angle of attack. In the Mach number range $0.865<M<0.89$, while neither case indicates a strong trend with angle of attack, the pulse and sweep results do appear to agree well. Thus it would appear that angle of attack is an important variable in determining flutter boundaries at high transonic Mach numbers and that transient and frequency sweep tests provide similar damping estimates if similar test conditions, including angle of attack, are considered.

Flutter Incident

As flight 3 progressed, there was no indication of problems in the operation of the FSS and no warning evident to the flutter test engineers that the FSS was operating at one-half nominal gain. The FSS-on test results for $M=0.775$ and 0.8

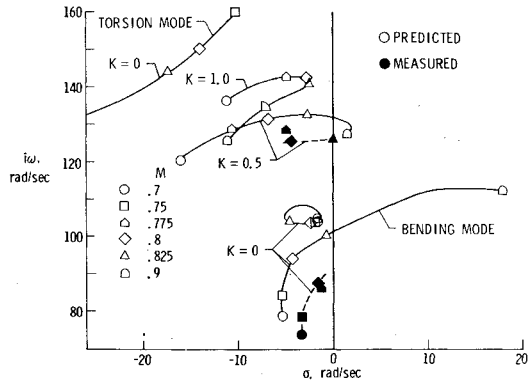

Fig. 11 Comparison of predicted and measured symmetrical root loci vs Mach number at $H=4.57$ km (15,000 ft) (open symbols denote predictions, closed symbols denote flight test results).

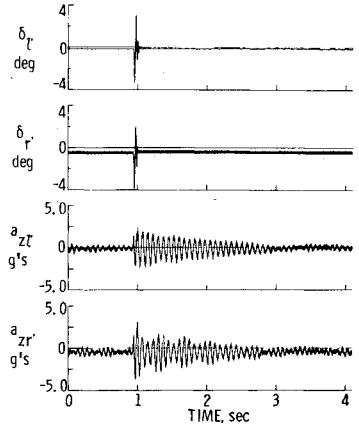

Fig. 12 Symmetric, open-loop response to pulse excitation at $M=0.907$ and $H=7.62$ km (25,000 ft).

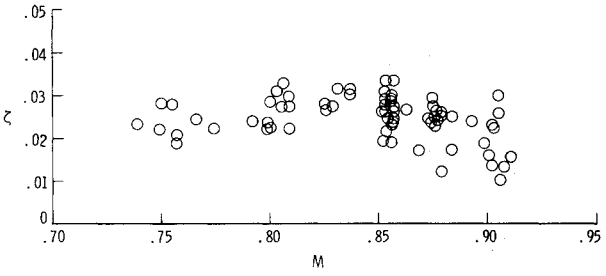

Fig. 13 Antisymmetric, open-loop damping estimates vs Mach number obtained from pulse responses at $M=7.62$ km (25,000 ft).

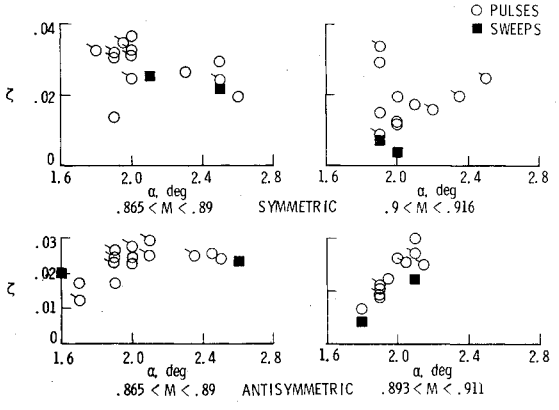

Fig. 14 Damping ratio estimates from FSS-off pulses vs angle of attack at $H=7.62$ km (25,000 ft) (flagged symbols denote estimates from high amplitude pulses, solid symbols denote estimates from frequency sweeps).

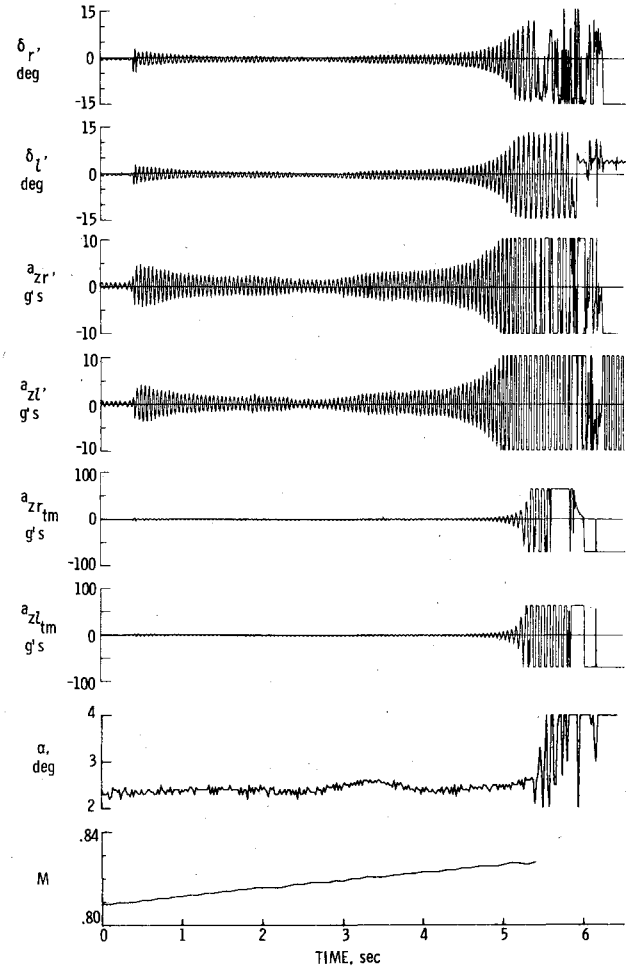

Fig. 15 Response following symmetric, FSS-on pulse excitation at $M \approx 0.825$ and $H = 4.57$ km (15,000 ft).

shown in Figs. 10 and 11 are similar to those anticipated for the full-gain FSS. In particular, the symmetric damping estimate at $M = 0.775$ was misleading, as described above, and had a better estimate been obtained at this Mach number, the trend toward a violent flutter condition would have been apparent at $M = 0.8$. Since the results appeared to agree with the nominal-gain predictions, which indicated a minimum damping condition near $M = 0.8$, clearance was given to $M = 0.825$.

During the acceleration from $M = 0.8$ to 0.825, several pulse responses were obtained showing increasingly lighter damping. The final pulse which preceded the flutter incident is shown in Fig. 15. Shown are the wing-tip FSS accelerometer signals, the wing-tip mass release accelerometer signals, and the aileron position signals, angle of attack, and Mach number. As this pulse response was observed, the test pilot was instructed to terminate the test. The throttle was retarded at the 2.5-s point and the motion on the angle-of-attack trace at 3 s is the result of pilot commands, but in the remaining seconds prior to the flutter incident the Mach number continued to increase. Mildly divergent oscillations at 20 Hz are seen at 3 s, where $M = 0.82$; and rapidly divergent oscillations occur at 4.5 s, where $M = 0.825$. Prior to the 5-s point, where the FSS accelerometers go off-scale, the oscillations doubled in amplitude in six cycles, corresponding to a negative damping of $\zeta = -0.02$. The ailerons saturated in amplitude two cycles later, followed by the firing of the tip mass release pyrotechnics at 5.2 s. (The automatic and manual tip mass release commands occurred nearly simultaneously.) The saturation of the ailerons resulted in an effective gain reduction and the effect upon the wing stability is shown in the $M = 0.85$ gain root locus of Fig. 3. The flutter mode frequency decreased from 20 to 15 Hz and the coupling with the 16-Hz fuselage bending mode is apparent in the oscillations seen in the angle-of-attack trace. The rate of growth of the oscillations was so large at the time of the operation of the tip mass release system that the oscillations were not arrested. Structural failure of the right wing tip and aileron occurred at 5.4 s, and at 5.6 s the structural attachment of right wing to the fuselage carry-through structure failed. The resulting rolling gyrations at large angles of attack and sideslip caused subsequent partial failure of the parachute recovery system and the vehicle impacted the ground. It has been concluded that the primary cause of the flutter incident was the error in gain setting. At the time of the incident all systems were functioning and the flutter suppression techniques applied to the ARW-1 appear capable of achieving the design goals. The decision has been made to rebuild the ARW-1 and complete the flutter test series to verify this. While the fuselage structure of the Firebee drone was damaged beyond repair, the wing spars and many of the avionics systems are reusable and the DAST ARW-1 is being reconstructed so that the flutter suppression experiment may be completed.

Concluding Remarks

Flight test results of the first three flights of an aeroelastic research wing have been described. The flight flutter test technique used to obtain near-real-time damping estimates from fast frequency sweep data was described and shown to be reliable for damping ratios less than 0.1. Exceptionally good flight test data was obtained and the open-loop flutter boundary determined. Apparently significant effects of angle of attack upon damping were observed at high transonic Mach numbers. An error in implementing the flutter suppression system resulted in a one-half nominal-gain configuration which caused the wing to be unstable at lower Mach numbers than anticipated and the vehicle experienced closed-loop flutter on its third flight.

References

[1] Murrow, H. N. and Eckstrom, C.V., "Drones for Aerodynamic and Structural Testing (DAST)—A Status Report," *Journal of Aircraft*, Vol. 16, Aug. 1979, pp. 521-526.

[2] Edwards, J. W. and Deets, D.A., "Development of a Remote Digital Augmentation System and Application to a Remotely Piloted Research Vehicle," NASA TN D-7941, April 1975.

[3] Newsom, J. R. and Pototsky, A. S., "Comparison of Analysis and Flight Test Data for a Drone Aircraft with Active Flutter Suppression," AIAA Paper 81-0640, Atlanta, Ga., 1981.

[4] Bennett, R. M. and Abel, I., "Application of a Flight Test and Data Analysis Technique to Flutter of a Drone Aircraft," AIAA Paper 81-0652, Atlanta, Ga., 1981.

[5] Visor, O.W. and Sevart, F.D., "Preliminary Design Study of Flutter Suppression Control System for BQM-34E/F Drone Aircraft with a Supercritical Wing—Final Report," NASA CR 145208, 1977.

[6] Bergmann, G.E. and Sevart, F.D., "Design and Evaluation of Miniature Control Surface Actuation Systems for Aeroelastic Models," *Journal of Aircraft*, Vol. 12, March 1975, pp. 129-134.

[7] Flutter Testing Techniques, NASA SP-415, 1976.

[8] van Nunen, J.W.G. and Piazzoli, G., "Aeroelastic Flight Test Techniques and Instrumentation," AGARD Flight Test Instrumentation Series, Vol. 9, AGARD-AG-160, Feb. 1979.

[9] Jennings, W.P., Olsen, N.L., and Walter, M. J., "Transient Excitation and Data Processing Techniques Employing the Fast Fourier Transform for Aeroelastic Testing," in *Flutter Testing Techniques*, NASA SP-415, 1976.

[10] Newman, K.W., Skingle, C.W., and Gaukroger, D.R., "The Development of Rapid-Testing Techniques for Flutter Experiments," ARC CP 1274, 1974.